

Switching Magnetism and Superconductivity with Spin-Polarized Current in Iron-Based Superconductor

Seokhwan Choi¹, Jong Mok Ok², Hyoung Joon Choi³, Won-Jun Jang^{4,5}, Alex Taekyung Lee⁶,
Young Kuk⁷, SungBin Lee¹, Andreas J. Heinrich^{4,5}, Sang-Wook Cheong⁸, Yunkyu Bang⁹,
Steven Johnston¹⁰, Jun Sung Kim², Jinhwan Lee^{1*}

¹ *Department of Physics, Korea Advanced Institute of Science and Technology, Daejeon
34141, Korea*

² *Department of Physics, Pohang University of Science and Technology, Pohang 37673,
Korea*

³ *Department of Physics and Center for Computational Studies of Advanced Electronic
Material Properties, Yonsei University, Seoul 03722, Korea*

⁴ *Center for Quantum Nanoscience, Institute for Basic Science (IBS), Seoul 03760, Korea*

⁵ *Physics Department, Ewha Womans University, Seoul 03760, Korea*

⁶ *Department of Applied Physics and Applied Mathematics, Columbia University, New York
10027, USA*

⁷ *Department of Physics and Astronomy, Seoul National University, Seoul 151-747, Korea*

⁸ *Rutgers Center for Emergent Materials and Department of Physics and Astronomy, Rutgers
University, Piscataway, New Jersey 08854, USA*

⁹ *Department of Physics, Chonnam National University, Kwangju 500-757, Korea*

¹⁰ *Department of Physics and Astronomy, University of Tennessee, Knoxville, Tennessee
37996-1200, USA*

Abstract

We have explored a new mechanism for switching magnetism and superconductivity in a magnetically frustrated iron-based superconductor using spin-polarized scanning tunneling microscopy (SPSTM). Our SPSTM study on single crystal $\text{S}_2\text{VO}_3\text{FeAs}$ shows that a spin-polarized tunneling current can switch the Fe-layer magnetism into a non-trivial C_4 (2×2) order, not achievable by thermal excitation with unpolarized current. Our tunneling spectroscopy study shows that the induced C_4 (2×2) order has characteristics of plaquette antiferromagnetic order in Fe layer and strongly suppressed superconductivity. This result suggests a new possibility of switching local superconductivity by changing the symmetry of magnetic order with spin-polarized and unpolarized tunneling currents in iron-based superconductors.

Main text

Iron-based superconductors (FeSCs) have shown intriguing phenomena related to the coexistence of magnetism and superconductivity below the superconducting transition temperature (T_c) [1-3]. Although understanding of their detailed interplay is still under debate, certain magnetic orders seem to be very crucial in realizing coexistent superconductivity [3-15]. Recent studies have shown new re-entrant C_4 symmetric antiferromagnetic phases (C_4 magnetism from now on) coexisting with superconductivity, and have reported that the superconducting T_c is suppressed due to the C_4 magnetic order [16-19]. A direct control of the Fe layer magnetic symmetry and the determination of its correlation with superconductivity at a fixed temperature well below optimal T_c may be useful for an in-depth understanding of the interplay between superconductivity and magnetism. To our knowledge, there has been no report of direct real-space observation of such a control by local probes and atomic scale demonstration of the correlation of magnetism and superconductivity.

In this regard, parent compound tetragonal iron-based superconductor $\text{Sr}_2\text{VO}_3\text{FeAs}$ with $T_c \approx 33$ K [20] is a good candidate where their interplay can be directly observed because of the possibility of multiple nearly degenerate magnetic ground states with different magnetic symmetries. $\text{Sr}_2\text{VO}_3\text{FeAs}$ has two types of square magnetic ion lattices: a square Fe lattice in the FeAs layer and a square V lattice in the two VO_2 layers sandwiching the FeAs layer as shown in Fig. 1(a). In their native states with optimal doping condition, FeAs layer usually prefers C_2 magnetism harboring superconductivity while VO_2 layer prefers C_4 magnetism [1-3,21]. The previous experimental results of $\text{Sr}_2\text{VO}_3\text{FeAs}$ [22-28] have often reported inconsistent results about magnetic order, but recent nuclear magnetic resonance measured in single crystal [29] and neutron scattering [30] experiments show that there is no long range magnetic order in V lattice at any temperature while the Fe lattice has C_2 magnetic order

consistent with superconductivity below 50 K. Meanwhile, a GGA+U calculation has suggested that there can be a number of low energy metastable magnetic states with different symmetries in V and Fe layers [21]. One plausible explanation is that in tetragonal $\text{Sr}_2\text{VO}_3\text{FeAs}$ the coupling between V and Fe layers plays a nontrivial role in the determination of the magnetic ground state among the multiple energetically close metastable states.

One possible way to explore the potentially frustrated magnetic states and their correlation to superconductivity is using a spin-polarized scanning tunneling microscope (SPSTM) to locally modify the magnetic environment with spin-polarized tunneling current. Our density functional theory (GGA+U) calculation (SM section 1) showed a possibility that a non-zero net spin density (experimentally in several nm^2 area under the tip induced by the injection of spin-polarized tunneling current) may lead to new balances among magnetic states with different symmetries as illustrated schematically in Fig. 1(b)-(e). The spin transfer torque and Joule heating effects of the spin-polarized tunneling current will then provide the energies to overcome the potential barriers between the different magnetic states [31].

In this letter, we demonstrate that a spin-polarized tunneling current can indeed drive the spin structure of Fe lattice into a nontrivial metastable C_4 magnetic order not usually achievable with thermal excitation. From the tunneling spectroscopy analysis measured inside and outside of the region of the induced C_4 magnetic order, we also find a signature of suppressed superconductivity in the C_4 order region, which is shown to be consistent with the nesting and spin fluctuation scenario of iron-based superconductivity.

We grew single crystals of $\text{Sr}_2\text{VO}_3\text{FeAs}$ with a self-flux method [29] which are then *in situ* cleaved at temperature ~ 15 K just before mounting on the STM head. Due to the weakly Van der Waals-coupled SrO-SrO layers, the cleaved surface is almost always terminated with symmetrically cleaved SrO layer as shown Fig. 1(a). For real-space magnetic imaging, we have

developed a technique of SPSTM with antiferromagnetic Cr-cluster tip (Cr-tip from now on) created *in situ* on a Cr(001) surface (SM section 2). Each Cr tip is confirmed on Cr(001) steps for spin contrasts (Fig. S2(c)) and no gap in the dI/dV spectrum on Cr(001) (Fig. S2(e)).

The 4.6 K STM topographic image on the as-cleaved SrO top layer of Sr₂VO₃FeAs taken with normal W tip in Fig. 2(c) shows small randomly oriented domains of quasi-C₂-symmetric atomic corrugations with no preference in any particular four-fold lattice direction in large scale, consistent with their identity as surface reconstruction (SR) in the absence of bulk orthorhombicity [30]. The SR also showed virtually no correlation with the superconducting gap map [32].

In contrast, our SPSTM images with spin-polarized Cr tip show, above a small bias threshold (~ 30 meV, ~ 25 pA), a C₄ symmetric (2 \times 2) order with intra-unit-cell topographic modulations (Fig. 2(d)-(e)) without any signature of SR seen in normal tip images (Fig. 2(c)). This implies that we have randomly fluctuating SR with flat time average (See Fig. S4) induced by the spin-polarized current and, at the same time, any magnetic signal of Fe-layer observed on the top layer oxygen should be the average of the four neighboring Fe spins connected to the As ions in each vertical O-V-As tunneling path as shown in Fig. 2(a) and (b). Hence the most natural explanation for the observed (2 \times 2) pattern with three groups of apparent height levels is the plaquette order in the Fe lattice with flat time-averaged SR. The Fourier-transformed q -space image (the inset of Fig. 2(d)) shows the double wave vectors $\mathbf{Q} = \left(\frac{\pi}{2}, \frac{\pi}{2}\right)_{Fe}$ and $\mathbf{Q}^* = \left(\frac{\pi}{2}, -\frac{\pi}{2}\right)_{Fe}$ expected from the plaquette order in Ref. 8.

To understand the nature of magnetic metastability in this system, we performed a comparative study of bias-dependent topographic measurements using normal (W) tip and spin-polarized (Cr) tip. In case of normal tip, as shown in Fig. 3(a)-(c), we found that the

surface starts to change at bias beyond $V_{th}^N \approx 300$ meV and the fluctuation becomes so rapid above 400 meV where the surface starts to appear essentially flat as a result of time-averaging of the fluctuations. Returning to the low bias condition as shown in Fig. 3(d), we observe that the square area which has experienced the high bias scanning has completely changed with sharply defined boundaries as shown in Fig. 4a.

On the other hand, in case of spin-polarized tip, as shown in Fig. 3(e)-(g), the surface looks identical to the normal tip case at low bias near 10 meV but the surface starts to change at a threshold bias about one order-of-magnitude smaller near $V_{th}^{SP} \approx 30$ meV, revealing the (2×2) domain structure and its phase domain walls. Returning to the low bias condition shown in Fig. 3(h), we could find that the C_4 order is still retained with extra fluctuations visible as random horizontal streaks. One plausible explanation is the presence of nearly degenerate metastable states with C_4 magnetic order whose energies are lowered below those of the pristine C_2 magnetic order states in presence of spin-polarized current. Its possibility is suggested by our model density functional theory (GGA+U) calculations with parameter set similar but not exactly the same as our experiment (See SM section 1).

To find the signature of any correlation between superconductivity and the C_4 magnetic order, we performed a comparative spectroscopic study as follows. We first acquired a large area topograph using a normal tip with bias condition below threshold V_{th}^N , then scanned over a smaller square area near the center (black dotted square in Fig. 4(a)) with bias condition exceeding the threshold V_{th}^N simulating the thermal annealing. Figure 4(a) is the topograph taken right afterwards with the bias condition below V_{th}^N again, and shows the changed surface topographic pattern which corresponds to another instance of the nearly degenerate ground states achievable by tunneling current-induced thermal annealing. Then we measured the dI/dV spectra inside (annealed) and outside (as-cleaved) of the central high-bias-scanned region. The

tunneling spectra measured both in the as-cleaved region (Fig. 4(c), green solid curve) and in the annealed area (Fig. 4(c), blue solid curve) show various identical features: a pair of peaks near -6 meV and $+6$ meV, and a SDW-gap-edge-like features near -18 meV and $+14$ meV. The ± 6 meV peaks are confirmed to be superconducting coherence peaks by its temperature dependence and by the fact that the temperature-dependent quasiparticle interference (QPI) data shows clearly the corresponding gap which closes near the bulk T_c and weakens at 7 Tesla magnetic field (Figs. 1 and S2 of Ref. 32 pdf supplied for Reviewer only) [32]. This result of comparison implies that the spectral features of dI/dV are contributed by the top-unit-cell FeAs layer deep beneath the surface SrO layer.

In the case of spin-polarized (Cr) tip, however, the results are qualitatively different. Fig. 4(b) shows a large area topograph taken with bias condition below V_{th}^{SP} after scanning over the smaller square region (black dotted square) with biases over V_{th}^{SP} (Fig. 3(e)-(g)). The central square region shows the well-defined C_4 domains (and various domain walls) induced by the spin-polarized current. The dI/dV spectra measured in the region with C_4 order (red and purple curves in Fig. 4(d)) shows that the superconducting coherence peaks and the SDW-gap-edge-like features are significantly suppressed in the presence of C_4 magnetic order.

One plausible explanation of the reason why the superconductivity is suppressed in this particular C_4 (plaquette) order is related to the mutual relationship of the spin wave dispersion in Fig. 2(f) (derived from Ref. 8) and the overlaid Fermi-surfaces observed in angle-resolved photoemission spectroscopy (ARPES) measurement [33]. For the C_4 (plaquette) order, the low energy spin fluctuations with wave vectors \mathbf{Q} and \mathbf{Q}^* do not satisfy the nesting condition between any pair of the Fermi surfaces Γ and M (X) and thus are unable to play the role of pairing boson effectively in the spin fluctuation-based theory of iron-based superconductivity. According to this scenario, this suppression of the nesting condition by the induced C_4 plaquette

orders will show a more drastic effect on superconductivity than switching between C_2 and C_4 orders maintaining the nesting conditions as shown in the recent studies on $\text{Ba}_{1-x}\text{K}_x\text{Fe}_2\text{As}_2$ [17] and $\text{Ba}_{1-x}\text{Na}_x\text{Fe}_2\text{As}_2$ where a more subtle T_c reduction was observed [18]. Among multiple theories of iron-based superconductivity based on spin fluctuations [34,35] and orbital fluctuations [36,37], our experimental results on this material seem to favor the former ones.

In summary, we provide a real-space signature of correlation between superconductivity and C_4 -magnetism in iron-based superconductor by changing the magnetic symmetry using spin-polarized STM. In this magnetically frustrated material, a spin-polarized tunneling current seems to be able to excite the spin structure of Fe lattice into a nontrivial metastable C_4 order not usually achievable with thermal excitation. We also found a spectroscopic signature of suppressed superconductivity in the C_4 order region induced by spin-polarized current which seems to agree with the nesting and spin fluctuation-based theories of iron-based superconductivity. Our findings may be extended in our future studies to manipulating superconductivity in a device made of magnetically frustrated few-layer heterostructure superconductor by changing the symmetry of the Fe-layer magnetism with the currents from ferromagnetic and non-magnetic electrodes.

Acknowledgement

The authors are thankful for helpful discussions with A. Chubukov, I. Mazin, H.-J. Lee, S.-J. Kahng, Ja-Yong Koo, C. Kim, J.J. Yu, W. Wu, K.-J. Kim, and J.H. Shim. This work was supported by the Metrology Research Center Program funded by Korea Research Institute of Standards and Science (No. 2015-15011069), the Pioneer Research Center Program (No. NRF-2013M3C1A3064455), the Basic Science Research Program (No. NRF-2017R1D1A1B01016186), the SRC Center Program for Topological Matter (No. 2011-0030046), the Creative Research Initiative Program (No. 2011-0018306) and the Brain Korea 21 Plus Program through the NRF of Korea, the Institute for Basic Science (IBS-R017-D1-2015-a00, IBS-R027-D1), the Max Planck POSTECH/KOREA Research Initiative Program (No. 2011-0031558) through the NRF and an NRF Program (2015R1C1A1A01052411) funded by MSIP of Korea, the Samsung Advanced Institute of Technology (SAIT), the Gordon and Betty Moore Foundation's EPiQS Initiative through Grant GBMF4413 to the Rutgers Center for Emergent Materials. Computational resources have been provided by KISTI Supercomputing Center (Project No. KSC-2016-C3-0052).

References

1. Johnston, D. C. The puzzle of high temperature superconductivity in layered iron pnictides and chalcogenides. *Adv. Phys.* **59**, 803-1061 (2010).
2. Hosono, H., Kuroki, K. Iron-based superconductors: Current status of materials and pairing mechanism. *Physica C* **514**, 399–422 (2015).
3. Dai, P. Antiferromagnetic order and spin dynamics in iron-based superconductors. *Rev. Mod. Phys.* **87**, 3 (2015).
4. Dai, P., Hu, J., Dagotto, E., Magnetism and its microscopic origin in iron-based high-temperature superconductors. *Nat. Phys.* **8**, 709-718 (2012).
5. Chandra, P., Coleman, P. & Larkin, A.I. Ising Transition in Frustrated Heisenberg Models. *Phys. Rev. Lett.* **64**, 88-91 (1988).
6. Chubukov, A. First-order transition in frustrated quantum antiferromagnets. *Phys. Rev. B* **44**, 392 (1991).
7. Glasbrenner, J. K., Mazin, I. I., Jeschke, H. O., Hirschfeld, P. J., Fernandes, R. M., Valentí, R., Effect of magnetic frustration on nematicity and superconductivity in iron chalcogenides, *Nat. Phys.* **11**, 953–958 (2015).
8. Ducatman, S., Perkins, N. B. & Chubukov, A. Magnetism in parent iron chalcogenides: Quantum fluctuations select plaquette order. *Phys. Rev. Lett.* **109**, 157206 (2012).
9. Villain, J., Bidaux, R., Carton, J.-P., Conte, R. Order as an effect of disorder. *J. Physique* **41**, 1263-1272 (1980).
10. Ma, F. and Lu, Z.-Y. Iron-based layered compound LaFeAsO is an antiferromagnetic semimetal, *Phys. Rev. B* **78**, 033111 (2008).

11. Dong, J. *et al.* Competing orders and spin-density-wave instability in $\text{La}(\text{O}_{1-x}\text{F}_x)\text{FeAs}$, *Europhys. Lett.* **83**, 27006 (2008).
12. Cvetkovic, V. and Tesanovic, Z. Valley density-wave and multiband superconductivity in iron-based pnictide superconductors, *Phys. Rev. B* **80**, 024512 (2009).
13. Vorontsov, A. B., Vavilov, M. G. and Chubukov, A. V. Superconductivity and spin-density waves in multiband metals, *Phys. Rev. B* **81**, 174538 (2010).
14. Eremin, I. and Chubukov, A. V. Magnetic degeneracy and hidden metallicity of the spin-density-wave state in ferropnictides, *Phys. Rev. B* **81**, 024511 (2010).
15. Balatsky, A. V., Basov, D. N. and Zhu, J. -X. Induction of charge density waves by spin density waves in iron-based superconductors, *Phys. Rev. B* **82**, 144522 (2010).
16. Avci, S. *et al.* Magnetically driven suppression of nematic order in an iron-based superconductor, *Nat. Comm.* **5**, 3854(2014).
17. Böhmer, A. E. *et al.* Superconductivity-induced re-entrance of the orthorhombic distortion in $\text{Ba}_{1-x}\text{K}_x\text{Fe}_2\text{As}_2$, *Nat. Comm.* **6**, 7911 (2015).
18. Wang, L. *et al.* Complex phase diagram of $\text{Ba}_{1-x}\text{Na}_x\text{Fe}_2\text{As}_2$: A multitude of phases striving for the electronic entropy. *Phys. Rev. B* **93**, 014514 (2016).
19. Allred, J. M. *et al.* Double-Q spin-density wave in iron arsenide superconductors, *Nat. Phys.* **12**, 493–498 (2016).
20. Zhu, X. *et al.* Transition of stoichiometric $\text{Sr}_2\text{VO}_3\text{FeAs}$ to a superconducting state at 37.2 K. *Phys. Rev. B* **79**, 220512 (2009).
21. Mazin, I. I. $\text{Sr}_2\text{VO}_3\text{FeAs}$ as compared to other iron-based superconductors. *Phys. Rev. B* **81**, 020507 (2010).
22. Tegel, M. *et al.* Possible magnetic order and suppression of superconductivity by V doping in $\text{Sr}_2\text{VO}_3\text{FeAs}$. *Phys. Rev. B* **82**, 140507 (2010).

23. Cao, G.-H. *et al.* Self-doping effect and successive magnetic transitions in superconducting Sr₂VFeAsO₃. *Phys. Rev. B* **82**, 104518 (2010).
24. Tatematsu, S., Satomi, E., Kobayashi, Y., Sato, M. Magnetic Ordering in V-Layers of the Superconducting System of Sr₂VFeAsO₃. *Jour. Phys. Soc. Jpn.* **79**, 123712 (2010).
25. Nakamura, H., Machida, M. Magnetic ordering in blocking layer and highly anisotropic electronic structure of high-*T_c* iron-based superconductor Sr₂VFeAsO₃: LDA+U study. *Phys. Rev. B* **82**, 094503 (2010).
26. Munevar, J. *et al.* Static magnetic order of Sr₄A₂O₆Fe₂As₂ (A = Sc and V) revealed by Mössbauer and muon spin relaxation spectroscopies. *Phys. Rev. B* **84**, 024527 (2011).
27. Garbarino, G. *et al.* Direct observation of the influence of the FeAs₄ tetrahedron on superconductivity and antiferromagnetic correlations in Sr₂VO₃FeAs. *Europhys. Lett.* **96**, 57002 (2011).
28. Ueshima, K. *et al.* Magnetism and superconductivity in Sr₂VFeAsO₃ revealed by ⁷⁵As- and ⁵¹V-NMR under elevated pressures. *Phys. Rev. B* **89**, 184506 (2014).
29. Ok, J. M. *et al.* Hidden order in a natural heterostructure of iron pnictides and vanadium oxides. In preparation.
30. Hummel, F., Su, Y., Senyshyn, A. & Johrendt, D. Weak magnetism and the Mott state of vanadium in superconducting Sr₂VO₃FeAs. *Phys. Rev. B* **88**, 144517 (2013).
31. Krause, S., Herzog, G., Schlenhoff, A., Sonntag, A., Wiesendanger, R. Joule Heating and Spin-Transfer Torque Investigated on the Atomic Scale Using a Spin-Polarized Scanning Tunneling Microscope. *Phys. Rev. Lett.* **107**, 186601 (2011).
32. Choi, S. *et al.* Correlation of Fe-Based Superconductivity and Electron-Phonon Coupling in an FeAs/Oxide Heterostructure. *ArXiv*:1608.00886.

33. Kim, Y.K., *et al.* Possible role of bonding angle and orbital mixing in iron pnictide superconductivity: Comparative electronic structure studies of LiFeAs and Sr₂VO₃FeAs. *Phys. Rev. B* **92**, 041116(R) (2015).
34. Mazin, I. I., Singh, D. J., Johannes, M. D., Du, M. H. Unconventional Superconductivity with a Sign Reversal in the Order Parameter of LaFeAsO_{1-x}F_x. *Phys. Rev. Lett.* **101**, 057003 (2008).
35. Fernandes, R. M., Chubukov, A. V. Low-energy microscopic models for iron-based superconductors: a review. *Rep. Prog. Phys.* **80**, 014503 (2017).
36. Kontani, H., Onari, S. Orbital-Fluctuation-Mediated Superconductivity in Iron Pnictides: Analysis of the Five-Orbital Hubbard-Holstein Model. *Phys. Rev. Lett.* **104**, 157001 (2010).
37. Saito, T. *et al.* Reproduction of experimental gap structure in LiFeAs based on orbital-spin fluctuation theory: s₊₊-wave, s_±-wave, and hole-s_±-wave states. *Phys. Rev. B* **90**, 035104 (2014).

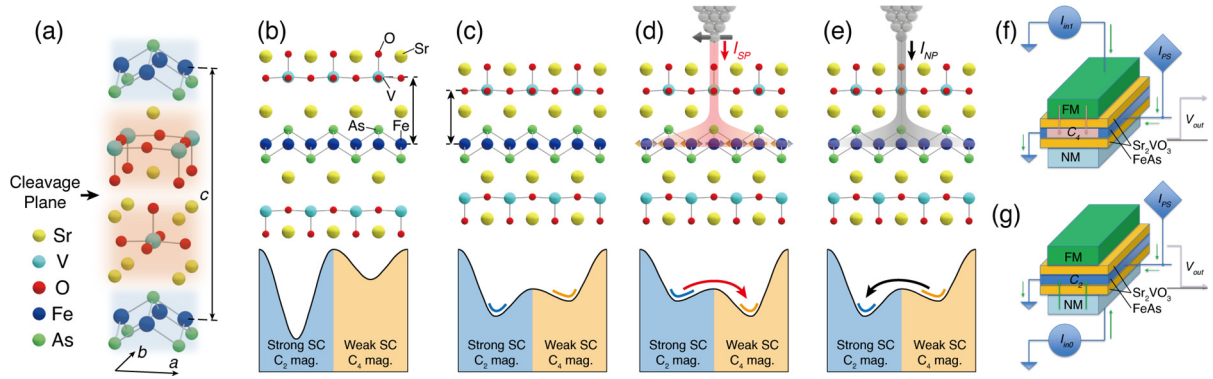


FIG 1. (a) A structural model of tetragonal $\text{Sr}_2\text{VO}_3\text{FeAs}$ lattice. Lattice constants are $a = b = 3.92 \text{ \AA}$ and $c = 15.6 \text{ \AA}$. (b-e) Schematic illustrations of FeAs-layer configuration potential landscapes for this material in various situations: (b) The imaginary case of FeAs and Sr_2VO_3 layers being separated sufficiently apart while the electron doping from Sr layer retained near optimal. The C_2 magnetism in Fe layer with strong superconductivity is preferred. (c) The realistic separation between FeAs and Sr_2VO_3 layers found in the actual single crystal results in near degeneracy among the magnetic states with different symmetries, with the C_2 magnetism with strong superconductivity still being the ground state. (d) If a sufficiently strong spin-polarized current is injected, the balances among these states may change, possibly resulting in C_4 magnetic states with weak superconductivity in the FeAs layer. (e) When an unpolarized spin current is injected, it can only simulate thermal agitation and will bring it back to the ground states with C_2 magnetism and strong superconductivity. (f-g) Conceptual diagrams of a device switching magnetism and superconductivity using currents from ferromagnetic (FM) and normal (NM) metal electrodes.

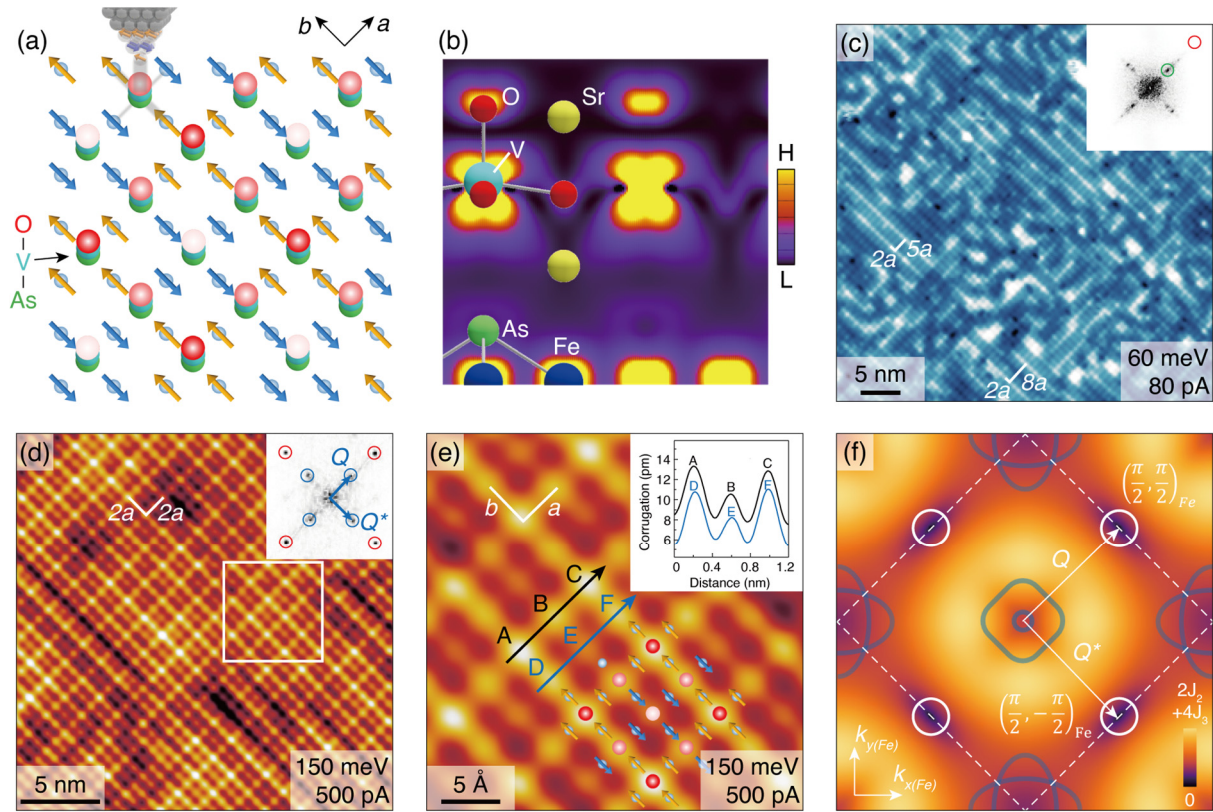


FIG 2. The Fe-layer C_4 magnetic order in $\text{Sr}_2\text{VO}_3\text{FeAs}$ activated and measured with spin-polarized tunneling current. (a) The structure of the Fe magnetic moments in the C_4 (plaque) order and the apparent (2×2) magnetic unit cell as a plausible explanation of our SPSTM measurements. Each red dot represents the oxygen at the top of each vertical O-V-As atomic chain, with the dot's redness indicating the net spin-polarized signal, determined by the average of the four neighboring Fe spins relative to the Cr tip spin. (b) The theoretical electron density plot near the Fermi level (integrated over $[-50, 0]$ meV), showing the existence of the vertical tunneling path made of O (top SrO layer) – V (VO_2 layer) – As (FeAs layer). (c) A typical 4.6 K STM topograph of cold-cleaved (~ 15 K) surface taken with W tip showing glassy C_2 surface reconstructions with random orientations. (d) A spin-polarized STM topograph taken with nearly-in-plane polarized Cr tip showing C_4 -symmetric (2×2) order. The insets of (c) and (d) are the respective Fourier-transformed (FT) images. The red, green, and blue circles in insets of (c) and (d) indicate Bragg peaks ($q = 2\pi/a$), SR peaks ($q = 16\pi/3a$), and Magnetic peaks

($q = \pi/a$) respectively. (e) The magnified view of the area in a white square in (d), with the (2×2) magnetic unit cells with a C_4 (plaquette) spin model overlaid. Inset shows topographic cross-sections along the black and blue arrows. (f) The spin wave dispersion of the C_4 spin order and the two momentum transfer vectors (\mathbf{Q} and \mathbf{Q}^*) from localized moment picture (Ref. 8), shown together with the ARPES-based Fermi surfaces (dark curves).

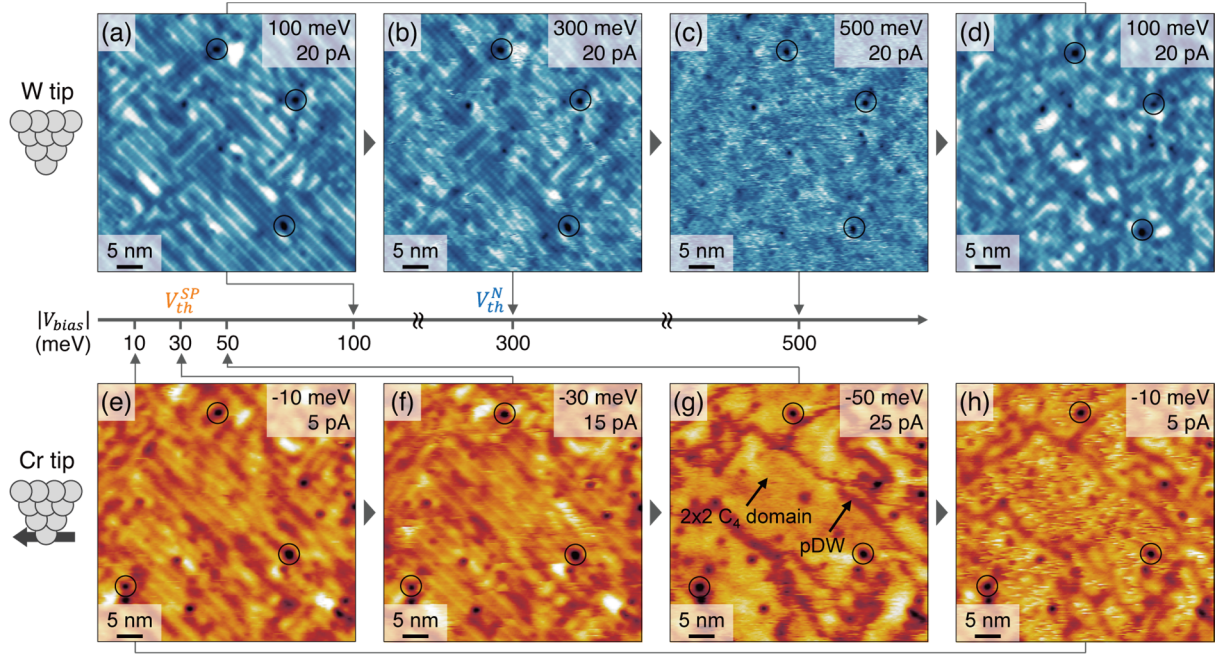


FIG 3. Tip-polarization-dependent metastable states excited with a normal (W) tip and a spin-polarized (Cr) tip taken at 4.6 K. (a-d) Bias dependence of normal tip topograph images. The threshold voltage for the fluctuation of the surface reconstruction is $V_{th}^N \approx 300$ meV. This may correspond to the case of Fig. 1(e) where only the C_2 magnetic states can be chosen. (e-h) Bias dependence of spin-polarized tip topograph images. A qualitative change occurs at a threshold one order-of-magnitude lower ($V_{th}^{SP}=30$ meV) where C_4 symmetric (2×2) domains and phase domain walls (pDW) are observed (g). This may correspond to the case of Fig. 1(d) where only the C_4 magnetic states can be chosen by the effect of spin-polarized tunneling current. The black circles indicate the identical locations in each group. Due to the low junction conductance, the individual (1×1) atomic lattice observed in Fig. 2(d)-(e) is weakened while the (2×2) modulation is still visible and its phases can be clearly resolved by changing the bias condition slightly (Fig. S6).

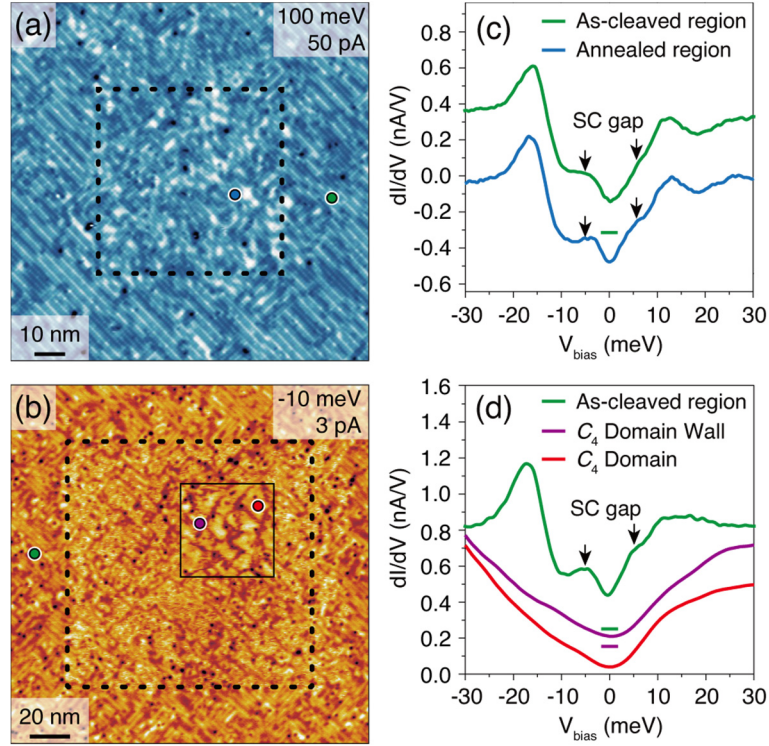


FIG 4. Tunneling spectroscopy on various regions with different metastable states excited using a normal tip and a spin-polarized tip at 4.6 K. (a)((b)) shows the W-tip (Cr-tip) topograph with bias conditions below threshold V_{th}^N (V_{th}^{SP}), measured after the intermediate scans shown in Fig. 3(a)-(c) (Fig. 3(e)-(g)) taken only in the area inside the dotted square. The inset image in the solid square in (b) is a Cr-tip topograph with higher bias above V_{th}^{SP} showing the domains and the domain walls more clearly (See Fig. S3). (c) ((d)) shows the tunneling spectra measured at marked positions with corresponding marker colors in (a) with a W tip ((b) with a Cr tip).

Supplemental Material for
**Switching Magnetism and Superconductivity with Spin-Polarized Current
in Iron-Based Superconductor**

Seokhwan Choi¹, Jong Mok Ok², Hyoung Joon Choi³, Won-Jun Jang^{4,5}, Alex Taekyung Lee⁶,
Young Kuk⁷, SungBin Lee¹, Andreas J. Heinrich^{4,5}, Sang-Wook Cheong⁸, Yunkyu Bang⁹,
Steven Johnston¹⁰, Jun Sung Kim², Jhinhwan Lee^{1*}

¹ *Department of Physics, Korea Advanced Institute of Science and Technology, Daejeon
34141, Korea*

² *Department of Physics, Pohang University of Science and Technology, Pohang 37673,
Korea*

³ *Department of Physics and Center for Computational Studies of Advanced Electronic
Material Properties, Yonsei University, Seoul 03722, Korea*

⁴ *Center for Quantum Nanoscience, Institute for Basic Science (IBS), Seoul 03760, Korea*

⁵ *Physics Department, Ewha Womans University, Seoul 03760, Korea*

⁶ *Department of Applied Physics and Applied Mathematics, Columbia University, New York
10027, USA*

⁷ *Department of Physics and Astronomy, Seoul National University, Seoul 151-747, Korea*

⁸ *Rutgers Center for Emergent Materials and Department of Physics and Astronomy, Rutgers
University, Piscataway, New Jersey 08854, USA*

⁹ *Department of Physics, Chonnam National University, Kwangju 500-757, Korea*

¹⁰ *Department of Physics and Astronomy, University of Tennessee, Knoxville, Tennessee
37996-1200, USA*

Correspondence*: jhinhwan@kaist.ac.kr

1. Theoretical study on metastability of C_4 magnetism induced by spin-polarized current

We used a first-principles pseudopotential method with the generalized gradient approximation to DFT, as implemented in the SIESTA code. For DFT calculations, we used the generalized gradient approximation to the exchange-correlation energy, pseudoatomic orbitals to expand the electronic wavefunctions, and semicore norm-conserving pseudopotentials for Sr, V, and Fe, as implemented in the SIESTA code. We used experimentally measured crystal structure of $\text{Sr}_2\text{VO}_3\text{FeAs}$. We included Sr 4s, Sr 4p, V 3s, V 3p, Fe 3s, and Fe 3p electrons as valence electrons. To describe the single-stripe and plaquette antiferromagnetic orderings, we used a $2 \times 2 \times 1$ supercell containing eight Fe atoms in a single FeAs layer.

We obtained the total energy of the system for the single-stripe and plaquette antiferromagnetic orderings of Fe magnetic moments. As shown in Fig. S1, the single-stripe antiferromagnetic ordering in the Fe layer is more stable than the plaquette ordering by about 80 meV/Fe when the sample has an equal number of spin-up and spin-down electrons, that is, the net ferromagnetic moment is zero. For V layers, we obtained that ferromagnetic ordering is stable within each V layer, with negligible magnetic coupling between adjacent V layers.

Then, in order to examine the experimental situation of having spin-polarized current injected from the STM tip to the sample, we considered breaking the number balance of the spin-up and spin-down electrons in our DFT calculations. As shown in Fig. S1, when we broke the number balance of the spin-up and spin-down electrons, that is, the net ferromagnetic moment was introduced to the system, the energy difference between the single-stripe and plaquette orderings decreased gradually. Finally, the plaquette ordering becomes more stable than the single-stripe orderings when the net ferromagnetic moment is larger than about one Bohr

magneton per formula unit. This result shows that the imbalance of the spin-up and spin-down electrons may stabilize the plaquette ordering and it supports our STM results with spin-polarized current, although it has only qualitative validity in the sense that such a large net moment might not occur in our STM experiment and, furthermore, the experimental situation is more complicated, with the presence of Cr atoms of the STM tip, strong local electric field from the tip, and deviation from equilibrium with net current.

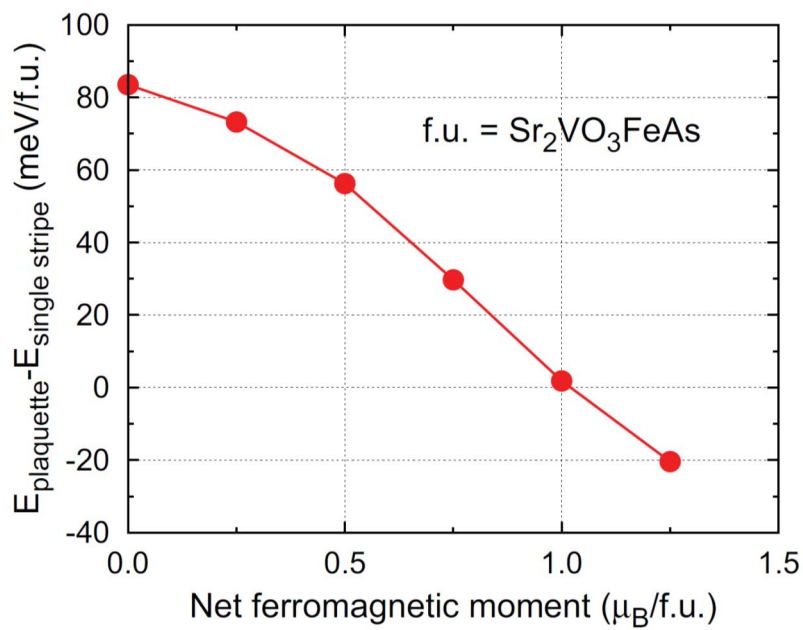


FIG S1. The total-energy difference between the plaquette and single-stripe antiferromagnetic orderings as a function of net ferromagnetic moment. The energy difference is in meV per formula unit ($\text{Sr}_2\text{VO}_3\text{FeAs}$) and the net ferromagnetic moment is in Bohr magneton per formula unit.

2. Preparation of Cr tip for SPSTM

The spin-polarized Cr cluster tip was prepared by collecting Cr atoms on the apex of the W tip by controlled field emission with parameters depending on the sharpness of the base W tip. The Cr cluster tip was then tested for proper in-plane spin-polarization by observing multiple levels of differential conductance at set point bias near -50 meV on multiple antiferromagnetic terraces with identical orientation on a stepped Cr surface as shown in Fig. S2.

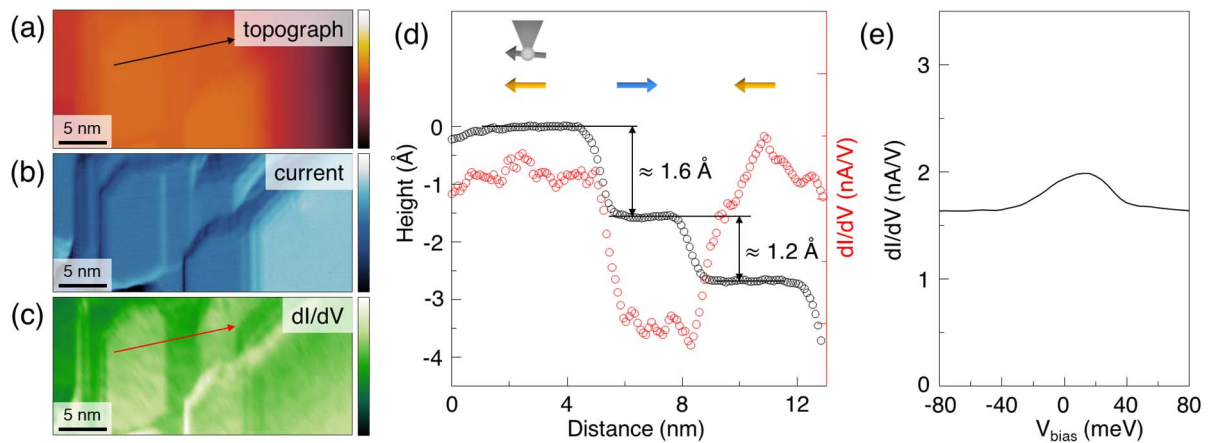


FIG S2. A sputter-annealed Cr(001) surface topograph (a), and simultaneously taken current image (b), and dI/dV image (c), at bias condition of $(-50$ mV, 200 pA). (c) The spin-contrast shown in cross-sections of topograph and dI/dV along a line marked with arrows in (a) and (c). (e) dI/dV spectrum taken with bias setpoint 1 nA, -200 meV on Cr(001) surface measured by Cr tip.

3. Near degeneracy of metastable C_4 order driven by spin-polarized tunneling current

In case of near degeneracy in metastable C_4 order made temporarily stable by spin-polarized tunneling current, we can expect to observe telegraphic noise in the tunneling current whose fluctuation rate decreases with decreasing bias voltage until it's too small compared with the energy difference between the two metastable states. As shown in Fig. S3 below, once the plaquette order is driven by strong spin-polarized tunneling current with bias voltage well over $V_{th}^{SP} \approx 30$ meV, significant amount of telegraphic noise begins to be observed which becomes clearer as the bias voltage is brought down below 30 meV due to the fluctuation rate decreasing below the preamp response frequency. The hysteresis of the topography as well as the telegraphic noise fluctuation rate due to metastability of the C_4 order is clearly visible as a function of the bias voltage.

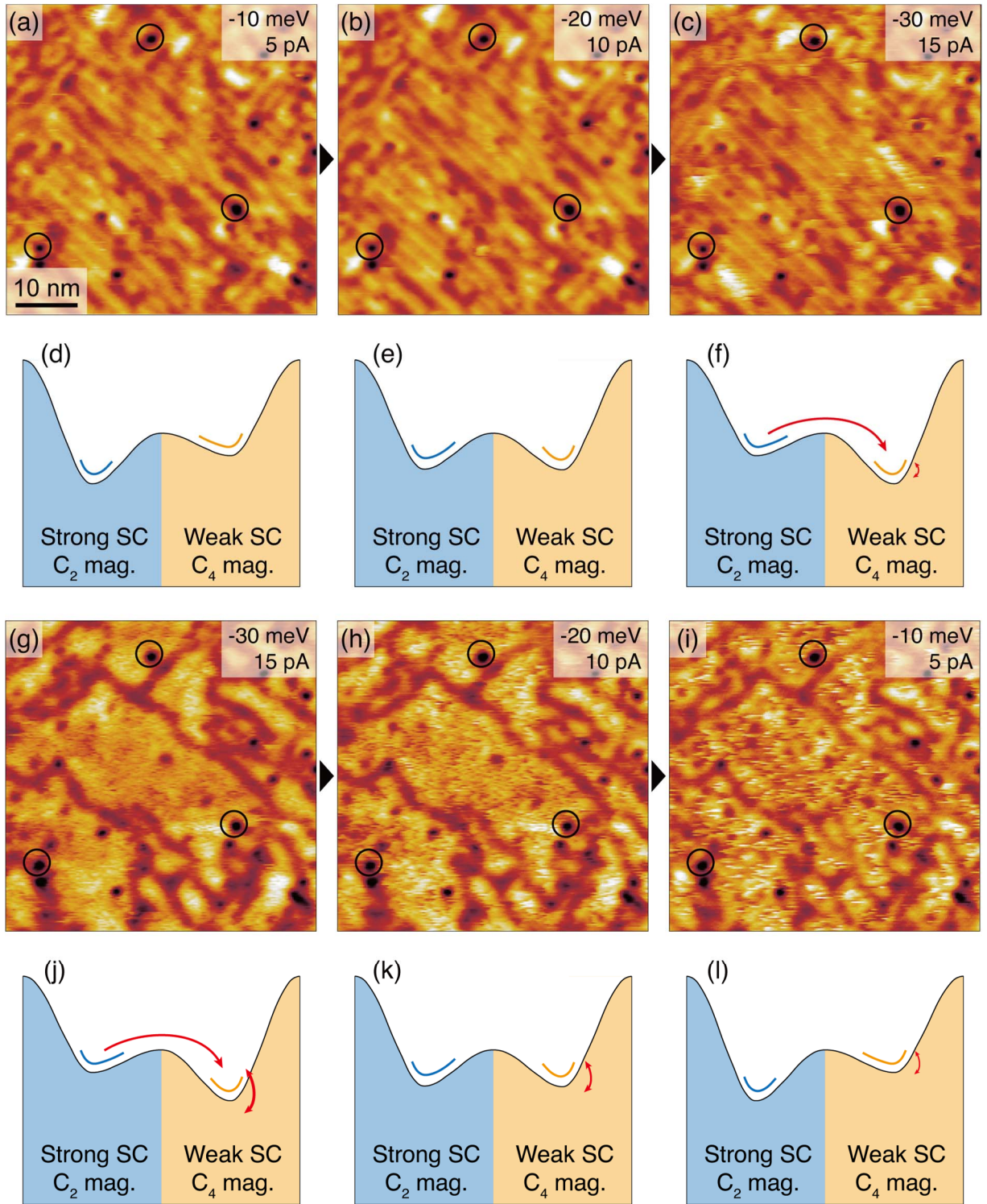


FIG S3. Evidence of near degeneracy of the metastable C_4 order driven by spin-polarized tunneling current. Once the bias voltage of the strong spin-polarized tunneling current is driven beyond $V_{th}^{SP} \approx 30$ meV, the C_4 order appears near the tip and is retained even when the bias voltage is reduced well below V_{th}^{SP} again. With the appearance of C_4 order, telegraphic noise

also appears and its rate increases with bias voltage and current which is an evidence of near degeneracy of the C_4 order.

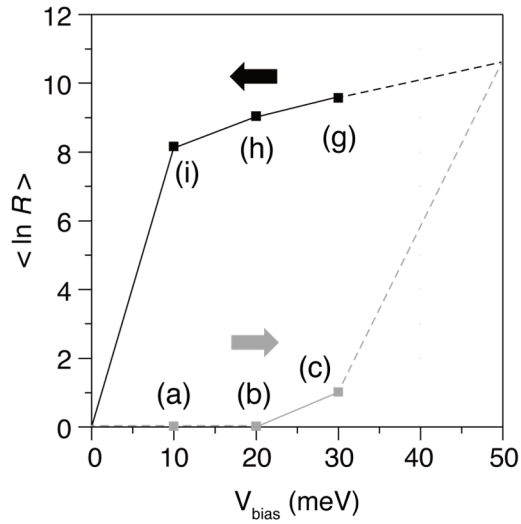


FIG S4. The rate of telegraphic noises showing bias hysteresis due to the tiny potential barriers of several meV's between the nearly degenerate states of the metastable C_4 order driven by spin-polarized tunneling current. (a)-(i) indicate the corresponding panels in Fig. S3.

4. SPSTM characteristics of Plaquette and other possible orders in $\text{Sr}_2\text{VO}_3\text{FeAs}$

In the Cr-cluster tip SPSTM imaging, the vertical tunneling conduction channel made of O-V-As to the Fe layer equally samples the spin polarization of the four Fe atoms neighboring of each As atom. When every four Fe spins underneath a particular O-V-As chain are parallel (antiparallel) to the Cr tip's spin polarization, the top layer O atom will look bright (dark) in the SPSTM topograph. On the other hand, if the four Fe spins underneath an O-V-As chain are grouped into two roughly parallel spins and two roughly antiparallel spins, they will possess neutral brightness just at the average of the brightness of the bright and the dark O atoms.

In this condition, the plaquette (ODS) order in Fe layer generates a (2×2) magnetic unit cell with characteristic intra unit cell pattern as simulated and shown in Fig. S5 (a). In contrast, the DDS (diagonal double stripe) order, the Néel order, the single stripe order, and the two kinds of spiral orders that may appear in the spin-order phase diagram for Heisenberg model have qualitatively different magnetic unit cells as shown in Fig. S5 (b)-(f).

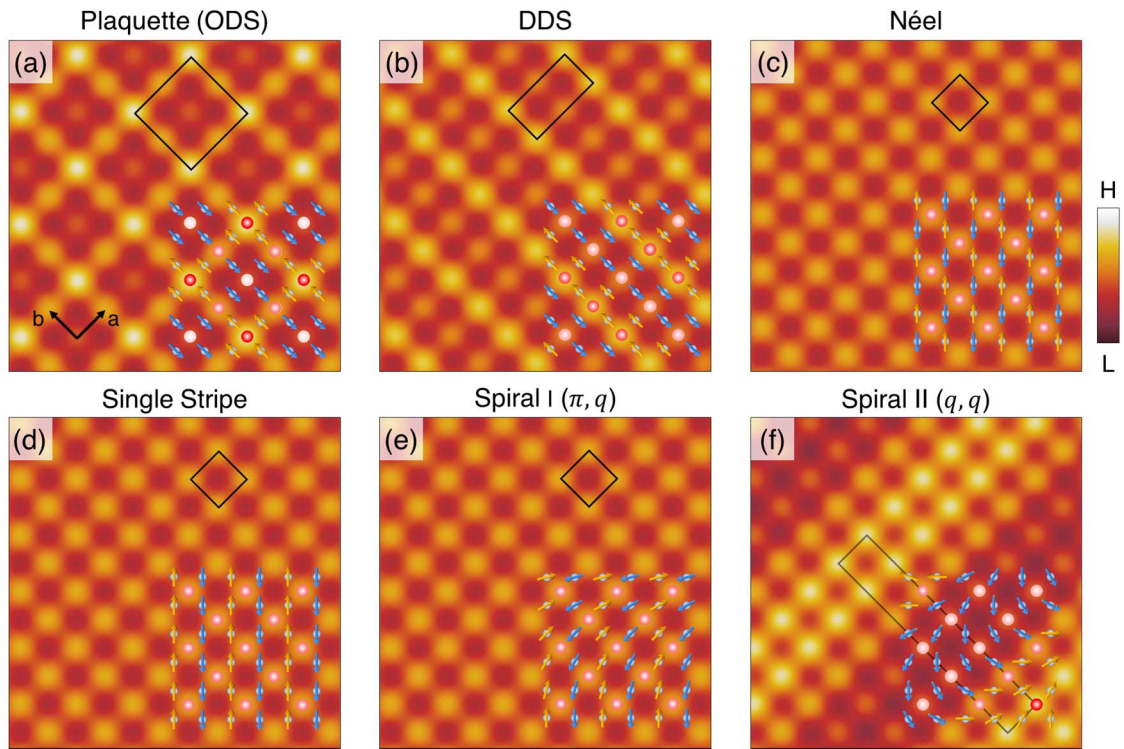


FIG S5. Simulated SPSTM topographs for various possible magnetic orders in the tunneling geometry of $\text{Sr}_2\text{VO}_3\text{FeAs}$. (a) Plaquette (orthogonal double stripe, ODS) order. (b) DDS (diagonal double stripe) order. (c) Néel order. (d) Single stripe order. (e) Spiral order 1 with wavevector (π, q) . (f) Spiral order 2 with wavevector (q, q) .

5. C_4 (2×2) phase domain walls visualized by spatial lock-in technique

The domain walls of the plaquette (ODS) order can be determined by first detecting the (2×2) spatial modulation phases ($\phi_a(\vec{r}), \phi_b(\vec{r})$) with a technique similar to the time-domain phase detection method known as the lock-in technique. To detect the modulation phase $\phi_a(\vec{r})$ in a -direction, we choose the Bragg peak position $\mathbf{q}_{(\pi,0)}$ corresponding to $(\pi, 0)$ in the Fourier Transform (FT) of the SPSTM topograph. We then generate two arrays S and C with identical size as the original topograph T , where S and C are filled with $\sin(\mathbf{q}_{(\pi,0)} \cdot \mathbf{r})$ and $\cos(\mathbf{q}_{(\pi,0)} \cdot \mathbf{r})$ respectively. Pixel-by-pixel multiplication of T and C denoted as C_T (and T and S denoted as S_T) contains fast spatial modulations with modulation wave vector near $2\mathbf{q}_{(\pi,0)}$ and slow spatial modulations with wave vector near 0. As with the time-domain lock-in technique, we filter out the fast $2\mathbf{q}_{(\pi,0)}$ modulations with a spatial low pass filter with cut off wave vector $\sim \mathbf{q}_{(\pi,0)}$ and denote them $\langle C_T \rangle$ and $\langle S_T \rangle$. Such $\langle C_T \rangle$ and $\langle S_T \rangle$ contain information of $A \cos \phi_a(\vec{r})$ and $A \sin \phi_a(\vec{r})$ respectively and the phase $\phi_a(\vec{r}) = \tan^{-1}(\langle S_T \rangle, \langle C_T \rangle)$ can be defined at every pixel of the topograph as shown in Fig. S6 (c). The domain walls (red curves in Fig. S6 (b)) determined by the spatial modulation phase shift in a -direction can then be defined as the collection of pixels with abrupt reversal (change by $\sim \pi$) of phase $\phi_a(\vec{r})$ within a magnetic unit cell distance from the pixel. Applying the identical method starting with the Bragg peak position $\mathbf{q}_{(0,\pi)}$ will generate $\phi_b(\vec{r})$ (Fig. S6 (d)) and the blue domain walls (blue curves in Fig. S6 (b)). The purple domain wall results from overlapping red and blue domain walls.

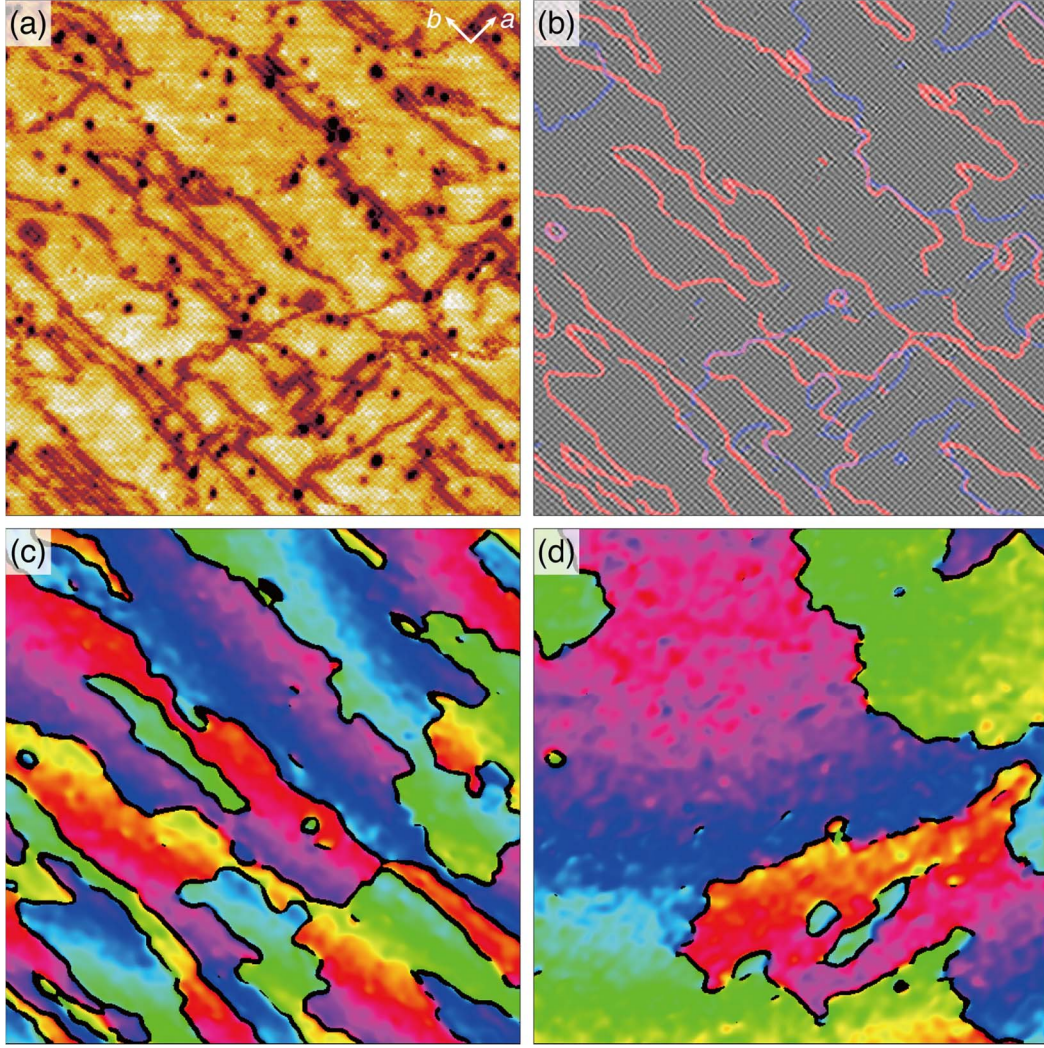


FIG S6. (a) Large area (71 nm x 71 nm) topograph taken at 4.6 K with spin-polarized Cr tip at bias condition of $(-50 \text{ meV}, 100 \text{ pA})$ on $\text{Sr}_2\text{VO}_3\text{FeAs}$. (b) Image of the automatically detected domain walls showing the (2×2) atomic modulations in each domain. The bright dots in each domain correspond to the brightest atom in the (2×2) unit cell. (c,d) The spatial modulation phase maps of $\phi_a(\vec{r})$ (c) and $\phi_b(\vec{r})$ (d), used to automatically detect the two types of domain walls. The piezo-creep-induced lattice distortion results in the slow variations of the phases over the field of view, which do not affect the domain wall detection algorithm relying on the abrupt phase change by π within the width ($\sim 2a$) of the domain walls.